

Abstract

The knowledge of Green House Gases GHGs fluxes at the air–sea interface at high resolution is crucial to accurately quantify the role of the ocean in the absorption and emission of GHGs. In this paper we present a novel method to reconstruct maps of surface ocean partial pressure of CO₂, $p\text{CO}_2$, and air–sea CO₂ fluxes at super resolution (4 km) using Sea Surface Temperature (SST) and Ocean Colour (OC) data at this resolution, and CarbonTracker CO₂ fluxes data at low resolution (110 km). Inference of super-resolution of $p\text{CO}_2$, and air–sea CO₂ fluxes is performed using novel nonlinear signal processing methodologies that prove efficient in the context of oceanography. The theoretical background comes from the Microcanonical Multifractal Formalism which unlocks the geometrical determination of cascading properties of physical intensive variables. As a consequence, a multiresolution analysis performed on the signal of the so-called singularity exponents allows the correct and near optimal cross-scale inference of GHGs fluxes, as the inference suits the geometric realization of the cascade. We apply such a methodology to the study offshore of the Benguela area. The inferred representation of oceanic partial pressure of CO₂ improves and enhances the description provided by CarbonTracker, capturing the small scale variability. We examine different combinations of Ocean Colour and Sea Surface Temperature products in order to increase the number of valid points and the quality of the inferred $p\text{CO}_2$ field. The methodology is validated using in-situ measurements by means of statistical errors. We obtain that mean absolute and relative errors in the inferred values of $p\text{CO}_2$ with respect to in-situ measurements are smaller than for CarbonTracker.

1 Introduction

The ocean can be thought of as a complex system in which a large number of different processes (e.g. physical, chemical, biological, atmosphere–ocean interactions) interacts with each other at different spatial and temporal scales (Rind, 1999). These

BGD

12, 1405–1452, 2015

Super-resolution CO₂ fluxes from Earth observations

I. Hernández-Carrasco et al.

Title Page

Abstract

Introduction

Conclusions

References

Tables

Figures

◀

▶

◀

▶

Back

Close

Full Screen / Esc

Printer-friendly Version

Interactive Discussion



scales extend from millimeters to thousands of kilometers and from seconds to centuries (Dickey, 2003). In particular, recently there is a growing body of evidence that the upper few hundred meters of the oceans are dominated by submesoscale activity, covering the range 1–10 km, and that this activity is important to understand global ocean properties (Klein and Lapeyre, 2009). Accurately estimating the sources and sinks of GHGs at the air–sea interface requires to solve these small scales (Mahadevan et al., 2004). However, the scarcity of oceanographic cruises and the lack of available satellite products for GHG concentrations at high resolution prevent from obtaining a global assessment of their spatial variability at small scales. For example, from the in-situ ocean measurements the uncertainty of the net global ocean–atmosphere CO₂ fluxes is between 20 and 30 % (IOCCP, 2007), and could be higher in the Oxygen Minimum Zones (OMZ) of the Eastern Boundary Upwelling Systems (EBUS) due to the extreme regional variability in these areas (Paulmier et al., 2008; Franco et al., 2014). This indeed suggests the design of proper methodologies to infer the fluxes at high resolution from presently available satellite images data, in order to improve current estimates of gas exchanges between the ocean and the atmosphere.

The most commonly used methods to estimate air–sea CO₂ fluxes are based either on statistical methods, inverse modeling with atmospheric transport models or global coupled physical-biogeochemical models. Let's cite here the work from Takahashi et al. (2002, 2009) where they interpolate sea surface *p*CO₂ measurements with advanced statistical methods to provide climatological monthly maps of air–sea fluxes of CO₂ in the global surface waters at a spatial resolution of 4° × 5°. Beside the Takahashi's works an international effort to compile global surface CO₂ fugacity (*f*CO₂) measurements has been recently performed and reported in Pfeil et al. (2013); Bakker et al. (2014), and later interpolated by Sabine et al. (2013) generating a monthly gridded product with *f*CO₂ values in a 1° × 1° grid cell. Gruber et al. (2009) used an inverse modeling of sources and sinks from the network of atmospheric CO₂ concentrations jointly with transport models. The third type of methods is based on the direct computations of the air–sea CO₂ fluxes in coupled physical-biogeochemical models incorporating the

BGD

12, 1405–1452, 2015

Super-resolution CO₂ fluxes from Earth observations

I. Hernández-Carrasco et al.

Title Page

Abstract

Introduction

Conclusions

References

Tables

Figures



Back

Close

Full Screen / Esc

Printer-friendly Version

Interactive Discussion



biogeochemical processes of the carbon dioxide system. In the latter, simulated surface ocean $p\text{CO}_2$ can be constrained with available ship observations as shown by Valsala and Maksyutov (2010).

Another new avenue to infer air–sea GHG fluxes is through inverse modeling applied to vertical column densities (VCD) extracted from satellite spectrometers, i.e. Greenhouse gases Observing SATellite (GOSAT) and SCIAMACHY, at low spatial resolution (Garbe and Vihharev, 2012). A global estimation of CO_2 fluxes in the ocean has been derived at $1^\circ \times 1^\circ$ of spatial resolution from global atmosphere observations used into a data assimilation system for CO_2 called CarbonTracker (Peters et al., 2007). In all these datasets the rather coarse spatial resolution leads to uncertainties in the actual estimate of the sources and sinks of GHGs, calling for an improvement of the resolution of CO_2 flux estimates.

In this regard, the last few years have seen the appearance of interesting new developments on multiscale processing techniques for complex signals coming from Earth Observations (Yahia et al., 2010). These methods make use of phenomenological descriptions of Fully Developed Turbulence (FDT) in nonlinear physics, motivated by the values taken on by Reynolds number in ocean dynamics. As predicted from the theory and also observed in the ocean, in a turbulent flow the coherent vortices (eddies) interact with each other stretching and folding the flow generating smaller eddies or small scale filaments and transition fronts characterized by strong tracer gradients (Frisch, 1995). This results in a cascade of energy from large to smaller scales. Therefore the inherent cascade of tracer variance under the turbulent flow dominates the variability of the geometrical distribution of tracers such as temperature or dissolved inorganic carbon, as shown by Abraham et al. (2000); Abraham and Bowen (2002); Turiel et al. (2005). Geometrical organization of the flow linked to the energy cascade allows to study its properties from the geometrical properties of any tracer for which the advection is the dominant process. The relationships between the cascade and the multifractal organization of FDT has been set up either in a canonical (Arneodo et al., 1995; Frisch, 1995) or microcanonical (Turiel et al., 2005; Bouchet and Venaille, 2012)

Super-resolution CO_2 fluxes from Earth observations

I. Hernández-Carrasco et al.

Title Page

Abstract

Introduction

Conclusions

References

Tables

Figures



Back

Close

Full Screen / Esc

Printer-friendly Version

Interactive Discussion



(Greenhouse gases Observing SATellite), in orbit since January 2009, to derive the air–sea flux. However SCIAMACHY and GOSAT sampling is not dense enough with very suboptimal sampling of the Benguela upwelling system. This led us to use data of CO₂ fluxes from CarbonTracker (<http://www.esrl.noaa.gov/gmd/ccgg/carbontracker/>) at spatial resolution of 1° × 1° (~ 110 km × ~ 110 km) (Peters et al., 2007). CarbonTracker system assimilates and integrates a diversity of atmospheric CO₂ data into a computation of surface CO₂ fluxes, using a state-of-the-art atmospheric transport model and an ensemble Kalman filter.

We obtain the partial pressure of ocean CO₂ by using the equation of the net flux in the air–sea interface:

$$F = \alpha K \left(p_{\text{CO}_2}^{\text{air}} - p_{\text{CO}_2}^{\text{ocean}} \right), \quad (2)$$

where α is the gas solubility, which depends on SST and Sea Surface Salinity SSS, and K , the gas transfer velocity, is a function of wind, salinity, temperature, sea state, which can be obtained from satellite data. To estimate the gas transfer velocity we use the well accepted relationships for the transfer velocity in air–sea gas exchange from wind speed, the parametrization developed by Sweeney et al. (2007). The CO₂ gas solubility is derived according to Weiss (1974). Input data for SST are derived from OSTIA product, SSS are derived from LEGOS product compiled by Delcroix et al. (2011) and winds from Cross Calibrated Multi-Platform Ocean surface winds from JPL PO.DAAC (<http://podaac.jpl.nasa.gov/>). We assume a $p_{\text{CO}_2}^{\text{air}}$ to be constant in the domain of study and it is derived from the Globalview-CO₂ product of the Cooperative Atmospheric Data Integration Project coordinated by Carbon Cycle Greenhouse Gases Group (www.esrl.noaa.gov/gmd/ccgg/globalview/). We use values taken at the closest station off Benguela, located at Ascension Island (7.97° S and 14.40° W).

The raw data of CarbonTracker fluxes of CO₂ in the area of interest are strongly binned and exhibit strong gradients across those bins. This turns out to be suboptimal for our super-resolution approach. For this reason, an approach similar to Garbe and

BGD

12, 1405–1452, 2015

Super-resolution CO₂ fluxes from Earth observations

I. Hernández-Carrasco et al.

Title Page

Abstract

Introduction

Conclusions

References

Tables

Figures

⏪

⏩

◀

▶

Back

Close

Full Screen / Esc

Printer-friendly Version

Interactive Discussion



Vihharev (2012) has been developed and applied to the CarbonTracker data set. However, the estimations are expensive and computing results for all the time frames of interest was infeasible. Therefore, an anisotropic diffusion-based approach has been applied to the raw fluxes of the CarbonTracker data set. The diffusion is steered by the direction of the low-altitude wind field. The results thus retain very well the structure of the CarbonTracker fluxes while suppressing artifacts. Results are comparable to the physically more accurate approach of Garbe and Vihharev (2012). Examples of this process are shown in Fig. 1.

2.2 Input data: satellite ocean data at high resolution

Oceanic $p\text{CO}_2$ is a complex signal depending, at any spatial resolution, on sea surface temperature, salinity, chlorophyll concentration, dissolved inorganic carbon, alkalinity and nutrients concentrations. Both the biological pump, with chlorophyll *a* as a proxy, and the physical pump, driven by the temperature and salinity (e.g. solubility, water mass), govern the evolution of $p\text{CO}_2$, when dealing with CO_2 for instance, in the surface ocean.

We use here the high resolution satellite ocean data for chlorophyll *a*, as a proxy for the biological carbon pump and for Sea Surface Temperature (SST), as a proxy for the thermodynamical pump, (see Sect. 3.2 for more details on the connection of these oceanic variables).

2.2.1 Chlorophyll *a* (Chl *a*) from Ocean Colour (OC)

In this study we use Chl *a* concentrations from two different Ocean Colour products: MERIS and GLOBCOLOUR. MERIS (MEDIUM RESOLUTION IMAGING SPECTROMETER INSTRUMENT) is on board the ENVISAT satellite and provides daily maps of ocean colour at $1/32^\circ$ (~ 4 km). Ocean colour from GLOBCOLOUR product is obtained by merging data provided by MODIS, MERIS and SeaWiFS instruments. The Chl *a* concentration is provided daily and at the spatial resolution equal to $1/32^\circ$ (~ 4 km). GLOB-

BGD

12, 1405–1452, 2015

Super-resolution CO_2 fluxes from Earth observations

I. Hernández-Carrasco et al.

Title Page

Abstract

Introduction

Conclusions

References

Tables

Figures

◀

▶

◀

▶

Back

Close

Full Screen / Esc

Printer-friendly Version

Interactive Discussion



COLOUR products are generated using different merging methods (see the GLOB-COLOUR Product User Guide document in http://www.globcolour.info/CDR_Docs/GlobCOLOUR_PUG.pdf):

- *Averaging from single-instrument chl a concentration*. In this case CHL1 daily level 3 (L3) products are generated for each instrument using the corresponding L2 data. At the beginning of the averaging process, an inter-calibration correction is applied to the MODIS and SeaWiFS CHL1 daily L3 products in order to get compatible concentrations with respect to the MERIS sensor. The merged CHL1 concentration is then computed as the average of the MERIS, MODIS and SeaWiFS quantities, both as: an *arithmetic mean* or a *weighted average value (AVW)*. In the AVW method, values of CHL1 are weighted by the relative error for each sensor on the results of the simple averaging.
- *Garver–Siegel–Maritorena model (GSM)*. In this method single-instrument daily L3 fully normalized water leaving radiances (individually computed for each band) and their associated error bars are used by the GSM model. These radiances are not inter-calibrated before incorporation in the model (see Maritorena and Siegel, 2005, for more details).

Snapshots of both Chl *a* fields derived from MERIS and GSM GLOBCOLOUR corresponding to 21 September 2006 are displayed in Fig. 2a and b, respectively. This example shows the clear difference in the remote sensing coverage between the two products. The merged GLOBCOLOUR product yields a more covered Chl field than the one obtained from MERIS. The merging algorithm in GLOBCOLOUR product tends to decrease the missing points induced by clouds for each individual instrument.

2.2.2 Sea Surface Temperature (SST)

We use SST derived from OSTIA and MODIS products. OSTIA (Operational SST and Sea Ice Analysis system) is a new analysis of SST that uses satellite data provided

BGD

12, 1405–1452, 2015

Super-resolution CO₂ fluxes from Earth observations

I. Hernández-Carrasco
et al.

Title Page

Abstract

Introduction

Conclusions

References

Tables

Figures



Back

Close

Full Screen / Esc

Printer-friendly Version

Interactive Discussion



- 2008, seven VOS cruises: *QUIMA2008-1*, *QUIMA2008-2*, *QUIMA2008-3*, *QUIMA2008-4*, *QUIMA2008-5*, *QUIMA2008-6*, *QUIMA2008-7*
- 2010, one cruise: *ANT27-1*

The small number of cruises found in one decade (24 cruises) shows that the scarcity of cruises in the Benguela region is a fact. This indeed demonstrates the crucial need of developing a robust method to infer high resolution $p\text{CO}_2$ from space. Moreover for some of these cruises, for instance, the track of GALATHEA cruise is too close to the coast and is out of the original CarbonTracker domain. Due to this restriction we only document the offshore conditions of this upwelling system. Owing to the relatively large number of cruises during 2005, 2006 and 2008 (a total of 20 cruises, representing 83 % of all available cruise data from 2000 through 2010), in this validation, we focus the analysis on the set of QUIMA-cruises during 2005 (QUIMA2005), 2006 (QUIMA2006) and 2008 (QUIMA2008) and we present the global analysis using all available cruises during these three years. Santana-Casiano et al. (2009) analyzed this data to study the sea surface $p\text{CO}_2$, $f\text{CO}_2$ and CO_2 air–sea fluxes offshore of the Benguela upwelling system between 2005 and 2006 (for each month from July 2005 up to November 2006) and González-Dávila et al. (2009) extended the study including cruises data from 2007 to 2008. The QUIMA line crosses the region between 5 and 35° S, with all the cruises following the same track.

3 Method

The idea hinges on the fundamental discovery of a simple functional dependency between the transitions – those being measured by the dimensionless values of the singularity exponents computed within the framework of the Microcanonical Multifractal Formalism – of the respective physical variables under study: SST, Ocean colour and oceanic partial pressure $p\text{CO}_2$. That functional dependency being adequately fitted

BGD

12, 1405–1452, 2015

Super-resolution CO_2 fluxes from Earth observations

I. Hernández-Carrasco et al.

Title Page

Abstract

Introduction

Conclusions

References

Tables

Figures



Back

Close

Full Screen / Esc

Printer-friendly Version

Interactive Discussion



into a linear regression model with good characteristics, it becomes possible to compute, at any given time, a precise evaluation of $p\text{CO}_2$ singularity exponents using SST, Ocean colour and low resolution acquired $p\text{CO}_2$. Once these singularity exponents are computed, they generate a multiresolution analysis from which low resolution $p\text{CO}_2$ can be cross-scale inferred to generate a high resolution $p\text{CO}_2$ product.

3.1 Singularity exponents and the multifractal hierarchy of turbulence

In the ocean, the turbulence causes the formation of unsteady eddies on many scales which interact with each other (Frisch, 1995). Most of the kinetic energy of the turbulent motion is contained in the large scale structures. The energy cascades from the large scale structures to smaller scale structures by an inertial and essentially inviscid mechanism. This process continues, creating smaller and smaller structures which produces a hierarchy of eddies. Moreover, the ocean is a system displaying scale invariant behavior, that is, the correlations of variables do not change when we zoom in or we zoom out the system, and can be represented by power-laws in particular, with the scaling exponents h .

It can be shown that the scaling exponents are the values taken on by localized singularity exponents, which can be computed at high precision in the acquired data using the Microcanonical Multifractal Formalism. Hence, within that framework, the multifractal hierarchy of turbulence, defined by a continuum of sets \mathcal{F}_h indexed by scaling exponents h , is obtained as the level sets of the geometrically localized singularity exponents.

We will not review here the details in the computation of the singularity exponents $h(\mathbf{x})$, leaving the reader to consult references (Turiel et al., 2005, 2008; Pont et al., 2011b; Maji and Yahia, 2014; Sudre et al., 2015) for an effective description of an algorithm able to compute the $h(\mathbf{x})$ at every point \mathbf{x} in a signal's domain.

Some examples of the singularity exponents of Chl and SST images for the different products described in Sect. 2.2 are shown in Figs. 2c and d and 3c and d, respectively. As compared to the corresponding images of Chl and SST showed in Figs. 2a and b

BGD

12, 1405–1452, 2015

Super-resolution CO_2 fluxes from Earth observations

I. Hernández-Carrasco
et al.

Title Page

Abstract

Introduction

Conclusions

References

Tables

Figures

⏪

⏩

◀

▶

Back

Close

Full Screen / Esc

Printer-friendly Version

Interactive Discussion



and 3a and b, one can see the ability of the singularity exponents to unveil the cascade structures arisen by tracer-gradient variances hidden in satellite images.

3.2 Functional dependencies between the singularity exponents of intensive physical variables

Another important idea implemented in the methodology is the coupling of the physical information contained in SST and OC images with the ocean $p\text{CO}_2$. For instance, it is known, that marine primary production is a key process in the oceanic carbon cycling, and variations in the concentration of phytoplankton biomass can be related to variations in the carbon concentrations. Surface temperature is also related with the gas solubility in the ocean, and areas with high temperatures are more suitable for releasing CO_2 to the atmosphere. We have studied the relationship of SST and Chl *a* variables with $p\text{CO}_2$ using the outputs of a coupled Regional Ocean Modeling System (ROMS) with the BIOgeochemical model of the Eastern Boundary Upwelling System (BIOEBUS) (Gutknecht et al., 2013). The ROMS includes several levels of nesting and composed grids, which makes it an ideal model for the basis of our methodology in working in two spatial resolutions. BIOEBUS has been developed for the Benguela to simulate the first trophic levels of the Benguela ecosystem functioning and also to include a more detailed description of the complete nitrogen cycle, including denitrification and anammox processes as well as the oxygen cycle and the carbonates system. This model coupled to ROMS has been also shown to be skillful in simulating many aspects of the biogeochemical environment in the Peru upwelling system (Montes et al., 2015). When one compares SST and Chl with $p\text{CO}_2$ one finds undetermined functional dependency. However, when comparing their corresponding singularity exponents one obtains a clear simpler dependency. This is due to the fact that SST, Chl and $p\text{CO}_2$ are variables of different dimensions while singularity exponents are dimensionless quantities.

These results show that there is a good correlation between the turbulent transitions given by the singularity exponents and that singularity exponents are good candidates

BGD

12, 1405–1452, 2015

Super-resolution CO_2 fluxes from Earth observations

I. Hernández-Carrasco
et al.

Title Page

Abstract

Introduction

Conclusions

References

Tables

Figures

◀

▶

◀

▶

Back

Close

Full Screen / Esc

Printer-friendly Version

Interactive Discussion



Super-resolution CO₂ fluxes from Earth observations

I. Hernández-Carrasco
et al.

Title Page

Abstract

Introduction

Conclusions

References

Tables

Figures



Back

Close

Full Screen / Esc

Printer-friendly Version

Interactive Discussion



are integral transforms that separate the relevant details of a signal at different scale levels, and since they are scale-tunable, they are appropriate to analyze the multiscale behavior of cascade processes and to represent them. However, as shown in Pottier et al. (2008); Yahia et al. (2010) and Pont et al. (2011a) not all multiresolution analyses are equivalent but the most interesting are those which are optimal with respect to inferring information along scales, in particular, in a context where information is to be propagated along the scales from low resolution to high resolution.

The effective determination of an optimal wavelet for a given category of turbulent signals is, in general, a very difficult open problem. This difficulty can be contoured by considering multiresolution analysis performed on the signal of the singularity exponents $h(\mathbf{x})$ themselves. Indeed, since the most singular manifold (the set \mathcal{F}_h associated to the lowest singularity exponents) is associated with the highest frequencies in a turbulent signal, and since the multifractal hierarchy \mathcal{F}_h converges to this set, it is physically evident that the multifractal hierarchy corresponds to a description of the detail spaces of a multiresolution analysis performed on a turbulent signal. Consequently, designing by V_j and W_j respectively the approximation and detail spaces computed on $\mathcal{S}(\rho\text{CO}_2)(\mathbf{x})$ signal, and by A_j and P_j their corresponding orthogonal projections from space $L^2(\mathbb{R}^2)$, the following reconstruction formula:

$$A_{j-1}\rho\text{CO}_2 = A_j\rho\text{CO}_2 + P_j h \quad (4)$$

consists in reconstructing a signal across the scales using the detail spaces of the singularity exponents, hence re-generating a physical variable according to its cascade decomposition. From these ideas, which are described more fully in the paper by Sudre et al. (2015), we can deduce the following algorithm for reconstructing a super-resolution ρCO_2 signal from available high-resolution SST, Chl a , and low-resolution ρCO_2 :

- Estimate linear regression coefficients $a(\mathbf{x})$, $b(\mathbf{x})$, $c(\mathbf{x})$ and $d(\mathbf{x})$ of Eq. (3) using a training set as described in Sect. 3.2.

- Given a time t and a low resolution signal ρCO_2 at time t , compute the singularity exponents $\mathcal{S}(\rho\text{CO}_2^{\text{LR}})$ at time t .
- Using Eq. (3), from available SST, Chl a data at time t , and $\mathcal{S}(\rho\text{CO}_2^{\text{LR}})$ at time t , compute $\mathcal{S}(\rho\text{CO}_2)$.
- Using Eq. (4) derive from the multiresolution analysis computed on signal $\mathcal{S}(\rho\text{CO}_2)$ and cross-scale inference on physical variable ρCO_2 at low-resolution, the physical variable ρCO_2 at the high-resolution of SST and Chl a .

The methodology has been successfully applied to dual ROMS simulation data at two resolutions, obtaining a mean absolute error of ρCO_2 reconstructed values with respect to ROMS simulated high-resolution ρCO_2 equal to $2.4 \mu\text{atm}$ (0.6 % of relative error) (V. Garçon, personal communication, 2014).

4 Preliminary analysis of Sea Surface Temperature (SST) and chlorophyll images

Since the key element for the application of our inferring algorithm relies on the ability in obtaining the singularity exponents and their quality, the success of our methodology applied to satellite data depends on the quality and the properties of the input data. In order to assess such properties we perform a statistical analysis of the different datasets. First, we analyze the Chl and SST Probability Distribution Functions (PDFs). In Fig. 4a we present the PDFs for Chl from MERIS, GLOBCOLOUR-GSM and GLOBCOLOUR-AVW; the required histograms are built using daily Chl values over 2006 and 2008 at each point of the spatial grid in the area of Benguela. Each one of these PDFs is broad and asymmetric, with a small mode (i.e. the value of Chl at which the probability reaches its maximum) between 0.1 and 0.2 mg m^{-3} and a heavy tail. The heavy tail (i.e. non-gaussianity) means that the extreme values can not be

neglected. In this case Chl values are mostly low (small mode) but there is a significant number of isolated and dispersed patches with very high Chl values producing intermittency (long tails in the PDF). Intermittency in the context of turbulence is the tendency of the probability distributions of some quantities to develop long tails, i.e. the occurrence of very extreme events.

Further information can be obtained by computing statistical quantities such as SD, skewness and kurtosis. Table 1 shows that SD is rather the same for the three OC products while skewness and kurtosis values hugely differ. The degree of intermittency is measured by the kurtosis, the higher the kurtosis, the higher the intermittency. We found that kurtosis is almost ten times higher in GLOBCOLOUR products than in MERIS.

We have repeated the same analysis for SST datasets. The PDFs of the SST values for OSTIA and MODIS products are shown in Fig. 4b. In this case both PDFs possess similar shape, broad with the mode around 18°C with a much less deviation from gaussianity as compared to Chl values. This is confirmed with the computation of the statistical moments showed in Table 1. We obtain small values of the SD and kurtosis in both cases, although slightly higher in the case of MODIS. The kurtosis is less than 3, meaning that there is not an important number of atypical values of SST and therefore weak and short tails in the PDFs.

If turbulence is dominated by coherent structures localized in space and time, then PDFs are not Gaussian, and the kurtosis will be higher than 3. To analyze this feature we turn to the statistical analysis of the singularity exponents, which, as explained before, have the ability to unveil the cascade structures given by the tracer gradients. In Fig. 4c, it can be seen that the PDFs of the singularity exponents of the Chl for the three products are rather similar with almost the same SD and with a slightly higher value of the kurtosis in the GLOBCOLOUR-GSM product, 4.3, than for MERIS, 3.1, and GLOBCOLOUR-AVW, 3.1, (see Table 2). This shows that Chl from GLOBCOLOUR-GSM product contains more extreme values which produce intermittency likely given by the strongest structures. The PDFs of the singularity exponents of the SST for OSTIA

BGD

12, 1405–1452, 2015

Super-resolution CO₂ fluxes from Earth observations

I. Hernández-Carrasco et al.

Title Page

Abstract

Introduction

Conclusions

References

Tables

Figures



Back

Close

Full Screen / Esc

Printer-friendly Version

Interactive Discussion



(Fig. 5b) at high resolution and $p\text{CO}_2$ at low resolution (Fig. 5c) derived from CarbonTracker air–sea flux of CO_2 (Fig. 5e) and using the Eq. (2). The air–sea flux of CO_2 at super-resolution (Fig. 5f) is obtained from the inferred $p\text{CO}_2$ field and a constant value of atmospheric $p\text{CO}_2$ equal to $385.6 \mu\text{atm}$. On this day the images of the inferred $p\text{CO}_2$ and fluxes of CO_2 combine a good coverage and a clear identification of small scale structures and gradients, as described below. Note that the air–sea CO_2 flux from CarbonTracker presents a large land mask close to the coast and consequently, we will rather study the offshore area of the Benguela upwelling. Comparing the figures one can see that values of $p\text{CO}_2$ and CO_2 flux over the domain (from 4.5°E to coast, taking out the mask of the CarbonTracker domain, and from 20.5 to 35°S) vary between 360 and $380 \mu\text{atm}$ and between -4×10^{-8} and $0.5 \times 10^{-8} \text{ mol C m}^{-2} \text{ s}^{-1}$, respectively. The resultant flux of CO_2 is positive (towards the atmosphere) in the region 25 – 28°S and from 7°E eastward to the coast and is negative (into the ocean) south of 30°S and east of 6°E . Thus, we see that in the southern part of the Benguela area there is a strong CO_2 sink and the northern part behaves as a weak CO_2 source.

What is new in the reconstructed $p\text{CO}_2$ is, for instance, that the cascade of information across the scales enhances gradients in the field of $p\text{CO}_2$. It is striking that the high-resolution map provides the position of the North–South dipole “front” located at 30°S (i.e. -1.5×10^{-8} isoline in green) which could not be inferred accurately from the low resolution map. The low resolution map would provide an estimate of the location of the “front” that is $\sim 1.5^\circ$ northern of the location inferred from the high-resolution map. Moreover one can see small structures in the inferred $p\text{CO}_2$ field between 33 – 35°S and 9 – 12°E in the inferred $p\text{CO}_2$ field (Fig. 5d). The small spatial scale variability is captured in the super-resolution $p\text{CO}_2$ field and not in CarbonTracker $p\text{CO}_2$ as shown in the longitudinal profile of the images plotted in Fig. 5 at latitude 33.5°S (see Fig. 6). The same high spatial variability given by the small scale structures of the SST and OC images can be appreciated in their corresponding longitudinal profiles displayed in the panel a and b of Fig. 6. It is worthy to note the change in the shape of the profiles between the inferred and CarbonTracker $p\text{CO}_2$ and fluxes of CO_2 at large scale, from

BGD

12, 1405–1452, 2015

Super-resolution CO_2 fluxes from Earth observations

I. Hernández-Carrasco
et al.

Title Page

Abstract

Introduction

Conclusions

References

Tables

Figures

◀

▶

◀

▶

Back

Close

Full Screen / Esc

Printer-friendly Version

Interactive Discussion



5.5 to 10.5° E, showing that the method not only introduces small scale features but also modifies the large scale spatial variability.

5.2 Evaluation of using different satellite products

Since the underlying aim of this work is to develop a methodology to infer super-resolution $p\text{CO}_2$ from space using remote observations, we perform a validation study of the different data used in the inferring computations. This provides us an evaluation of which satellite products are more suitable for our methodology and thus a gain in confidence in our method as well as a better understanding of its limitations. The evaluation analysis is addressed taking into account two main concerns: one related to the number of valid points yielded in the inferred $p\text{CO}_2$ field, and another with regard to the degradation of the information contained in the transition fronts. A valid point is a pixel where we have simultaneously Chl, SST and $p\text{CO}_2$ values from CarbonTracker, from which we can obtain a value of inferred $p\text{CO}_2$, in other words without missing information. One example comparing the reconstructed $p\text{CO}_2$ field obtained from the mentioned above three products combinations is plotted in Fig. 7. The general pattern is quite similar in all of them with some differences in the details of the small scales and in the missing points due to cloudiness (white patches). This example clearly shows how different can be the coverage of the $p\text{CO}_2$ field depending on the products combination.

Similar results are found when one compares the spatial distribution of time average over 2006 and 2008 of the reconstructed $p\text{CO}_2$ values for the three product combinations (Fig. 8). The same pattern with an area of higher $p\text{CO}_2$ between 24 and 30° S and lower $p\text{CO}_2$ values outside this region is produced with the three combinations. The most noticeable differences are located in the most northern region and in the south-eastern region off Benguela. This can be quantified by computing the SD of the reconstructed $p\text{CO}_2$ values among the different combination of datasets. Figure 8d shows the spatial distribution of the time average over 2006 and 2008 of the SD computed in each pixel among the inferred $p\text{CO}_2$ values obtained from the three products

combinations. The larger values of the dispersion (not greater than 5 μatm) are found in the northern region from 23° S to the north and in the southern region, in particular, in the area from 31.5° S to the south and from 11° E to the east. The low value of the dispersion indicates that the method is robust when different datasets are used in the inference.

First, we compute the number of valid points in the inferred $p\text{CO}_2$ field for each product combination. Table 3 summarizes the total number of valid points for each products combination for both years 2006 and 2008. As expected, the number of valid points is found to be the highest for the combination of merged products OSTIA SST and GLOBCOLOUR-GSM with $N_{\text{GO}} = 27\,313\,043$ points, followed by the combination MODIS SST and GLOBCOLOUR Chl with $N_{\text{MG}} = 20\,397\,047$ points and finally by the OSTIA SST and MERIS Chl combination with $N_{\text{OM}} = 9\,800\,776$ points. Looking at the different proportions, we find that the number of valid points is 2.78 times larger when using the merged products OSTIA and GLOBCOLOUR-GSM than using OSTIA and MERIS, 1.33 times larger than using MODIS and GLOBCOLOUR-GSM and 1.08 times larger using OSTIA SST and GSM Chl a than using MODIS SST and GSM Chl a . Further, if we know that the total number of pixels in the domain taking out the points of the CarbonTracker mask and for the two years is $N_p = 55\,711\,378$, one can estimate the loss of valid points for each combination, LP_x . LP_x is computed by dividing the relative difference between the number of total available pixels in the domain N_p and the number of points in the inferred $p\text{CO}_2$ field obtained for each product combination, N_x , with respect to the total number of pixels N_p , $\text{LP}_x = \frac{N_p - N_x}{N_p} 100\%$. Here the subscript x refers to the product combination (e.g. $\text{LP}_x = \text{LP}_{\text{OM}}$, LP_{OG} and LP_{MG} for the loss of valid points with the OSTIA-MERIS, OSTIA-GLOBCOLOUR and MODIS-GLOBCOLOUR products combination, respectively). The loss of valid points due to cloudiness in the ocean colour and SST images is less severe for the OSTIA-GLOBCOLOUR combination with a loss of 51 % and being the more affected by the cloudiness the OSTIA-MERIS combination with a loss of 82 %.

Super-resolution CO_2 fluxes from Earth observations

I. Hernández-Carrasco
et al.

[Title Page](#)[Abstract](#)[Introduction](#)[Conclusions](#)[References](#)[Tables](#)[Figures](#)[◀](#)[▶](#)[◀](#)[▶](#)[Back](#)[Close](#)[Full Screen / Esc](#)[Printer-friendly Version](#)[Interactive Discussion](#)

Super-resolution CO₂ fluxes from Earth observations

I. Hernández-Carrasco
et al.

Title Page

Abstract

Introduction

Conclusions

References

Tables

Figures



Back

Close

Full Screen / Esc

Printer-friendly Version

Interactive Discussion



Next we explore the quality of the information contained in the transition fronts, in particular, in the non-merged products such as MERIS OC and MODIS SST as compared to the merged products: GLOBCOLOUR OC and OSTIA SST. The PDFs of $p\text{CO}_2$ values from CarbonTracker and inferred $p\text{CO}_2$ values for the three combinations of OC and SST products, i.e. MERIS-OSTIA, GLOBCOLOUR-OSTIA, MODIS-GLOBCOLOUR (see Fig. 9) show that there is a good correspondence of all inferred $p\text{CO}_2$ values with those from CarbonTracker. Indeed the histograms show also a better agreement between merged products and CarbonTracker: the peak of the PDF for inferred $p\text{CO}_2$ is closer to CarbonTracker peak in the case of OSTIA and GLOBCOLOUR than when using MERIS and MODIS products.

Furthermore, to analyze the realism of the transitions fronts for the different products we compute the singularity spectra for the three product combinations (see Fig. 10). One can see that at low values of h (singularity exponent), related to the most singular manifolds, the shape of singularity spectrum for inferred data from merged products better matches a binomial cascade, with an improved description of the dimension of the sharpest transition fronts. We know from the theory, that tracers advected by the flow in the turbulent regime, as it happens in the ocean, shows a multifractal behavior with a characteristic singularity spectrum $D(h)$ similar, for some types of turbulence, to $D(h)$ for the binomial multiplicative process.

5.3 Validation with in-situ measurements

Next, we perform a validation analysis of the results of our algorithm to infer $p\text{CO}_2$ at super-resolution with field observations of oceanic $p\text{CO}_2$. In particular we perform the validation using $p\text{CO}_2$ ocean data from in-situ measurements taken in the Benguela region (see Sect. 2.3). We decided to carry out directly the validation on $p\text{CO}_2$ rather than on the air–sea CO₂ flux since the field measurements do provide oceanic $p\text{CO}_2$ data.

From now on we are going to use the following notation for the three different sources of $p\text{CO}_2$: we refer to the values of ocean $p\text{CO}_2$ derived from CarbonTracker

as $p\text{CO}_2^{\text{Ctrack}}$, values of inferred $p\text{CO}_2$ at higher resolution from $p\text{CO}_2$ at low resolution together with computation of the cascade onto SST and chlorophyll *a* concentration as $p\text{CO}_2^{\text{infer}}$, and finally $p\text{CO}_2^{\text{insitu}}$ refers to the values of the in-situ measurements of $p\text{CO}_2$.

An example of the qualitative comparison of values of $p\text{CO}_2^{\text{Ctrack}}$, $p\text{CO}_2^{\text{infer}}$ for all the products combinations and $p\text{CO}_2^{\text{insitu}}$ at the intersections of the QUIMA cruise during 4–7 July 2008, as a function of the longitudinal coordinate of the intersections, is shown in Fig. 11. While there are visible differences between various $p\text{CO}_2$ values, the values of $p\text{CO}_2^{\text{infer}}$ approximate better $p\text{CO}_2^{\text{insitu}}$ values than those of $p\text{CO}_2^{\text{Ctrack}}$. The small scale patterns are well reproduced in the inferred $p\text{CO}_2$ field. Values of $p\text{CO}_2^{\text{infer}}$ exhibit gradients and small scale fluctuations, likely induced by the presence of fronts, which can be also detected on the profile of the in situ measurements of $p\text{CO}_2$. Most of days $p\text{CO}_2^{\text{infer}}$ and $p\text{CO}_2^{\text{Ctrack}}$ values overestimate $p\text{CO}_2^{\text{insitu}}$ values. In some days, $p\text{CO}_2^{\text{infer}}$ values follow the same trend, with the same small scale fluctuations than $p\text{CO}_2^{\text{insitu}}$.

First, we analyze the number of valid intersections for each product combination. A valid intersection is a placement in space and time common to the inferred, CarbonTracker and in-situ $p\text{CO}_2$, without missing values. On one hand, among the 20 available cruises in the Benguela through 2005, 2006 and 2008 we find that the total number of in-situ measurements in the Benguela region under study is $N_{\text{insitu}} = 17\,355$ and within the CarbonTracker domain this number is reduced to $N_{\text{Ctrack}} = 8377$ measurements. To estimate the loss of valid intersections due to the land mask of of the CarbonTracker we compute the relative difference of the number of intersections between the cruise trajectories and the CarbonTracker domain with respect to the number of the in-situ measurements, $L_{\text{Ctrack}} = \frac{N_{\text{insitu}} - N_{\text{Ctrack}}}{N_{\text{insitu}}} 100\% = 52\%$, showing that half of the measurements is geographically in the coastal region of Benguela, outside the CarbonTracker domain.

The number of valid intersections is the largest with the OSTIA-GLOBCOLOUR combination (Table 4). To quantify the loss of valid intersections between the in-situ measurements and points in the $p\text{CO}_2^{\text{infer}}$ field, likely due to the cloudiness, we

Super-resolution CO_2 fluxes from Earth observations

I. Hernández-Carrasco
et al.

[Title Page](#)[Abstract](#)[Introduction](#)[Conclusions](#)[References](#)[Tables](#)[Figures](#)[⏪](#)[⏩](#)[◀](#)[▶](#)[Back](#)[Close](#)[Full Screen / Esc](#)[Printer-friendly Version](#)[Interactive Discussion](#)

compute the relative difference between the number of measurements into the CarbonTracker domain and the valid points in the inferred $p\text{CO}_2$ field with respect to the number of intersections measurements of each cruise and the $p\text{CO}_2^{\text{Ctrack}}$ field, $L_{\text{infer}} = \frac{N_{\text{Ctrack}} - N_{\text{infer}}}{N_{\text{Ctrack}}} 100\%$. We repeat such a computation for the three product combinations. The percentage of losses of intersections in inferred field L_{infer} becomes twice as large than in the case of the OSTIA-SST and MERIS-Chl combination, and even higher than with the CarbonTracker domain mask.

In order to study quantitatively the difference between values of $p\text{CO}_2^{\text{Ctrack}}$ and $p\text{CO}_2^{\text{infer}}$ with respect to $p\text{CO}_2^{\text{insitu}}$ measurements we compute the following statistical quantities:

- *Mean Error (ME)*: average over all the intersections of the difference between $p\text{CO}_2^{\text{Ctrack}}$, $p\text{CO}_2^{\text{infer}}$ and $p\text{CO}_2^{\text{insitu}}$ at the same intersection, i ,

$$\text{ME}_{\text{Ctrack}} = \frac{1}{N} \sum_{i=1}^N \left(p\text{CO}_2^{\text{Ctrack}}(i) - p\text{CO}_2^{\text{insitu}}(i) \right) \quad (5)$$

$$\text{ME}_{\text{infer}} = \frac{1}{N} \sum_{i=1}^N \left(p\text{CO}_2^{\text{infer}}(i) - p\text{CO}_2^{\text{insitu}}(i) \right), \quad (6)$$

where N is the number of intersections.

- *Mean Absolute Error (AE)*: average over all the intersections of the absolute values of the difference between $p\text{CO}_2^{\text{Ctrack}}$ or $p\text{CO}_2^{\text{infer}}$ and $p\text{CO}_2^{\text{insitu}}$ at the same

Super-resolution CO₂ fluxes from Earth observations

I. Hernández-Carrasco et al.

Title Page

Abstract

Introduction

Conclusions

References

Tables

Figures



Back

Close

Full Screen / Esc

Printer-friendly Version

Interactive Discussion



intersection,

$$AE_{\text{Ctrack}} = \frac{1}{N} \sum_{i=1}^N \left| p\text{CO}_2^{\text{Ctrack}}(i) - p\text{CO}_2^{\text{insitu}}(i) \right| \quad (7)$$

$$AE_{\text{infer}} = \frac{1}{N} \sum_{i=1}^N \left| p\text{CO}_2^{\text{infer}}(i) - p\text{CO}_2^{\text{insitu}}(i) \right| \quad (8)$$

– *Mean Relative Error (RE)*: average over all the intersections of the errors of the estimated values of $p\text{CO}_2$ (CarbonTracker or inferred) with respect to the reference $p\text{CO}_2$ values (in-situ) at the same intersection,

$$RE_{\text{Ctrack}} = \frac{1}{N} \sum_{i=1}^N \left| \frac{p\text{CO}_2^{\text{Ctrack}}(i) - p\text{CO}_2^{\text{insitu}}(i)}{p\text{CO}_2^{\text{insitu}}(i)} \right| \quad (9)$$

$$RE_{\text{infer}} = \frac{1}{N} \sum_{i=1}^N \left| \frac{p\text{CO}_2^{\text{infer}}(i) - p\text{CO}_2^{\text{insitu}}(i)}{p\text{CO}_2^{\text{insitu}}(i)} \right| \quad (10)$$

We started the statistical validation by analyzing each QUIMA cruise separately (not shown) and we found that in most of the cruises, the absolute error for inferred $p\text{CO}_2$ is relatively small (less than $15 \mu\text{atm}$) except on 21 August 2006 and 17 May 2008 with an error of 44 and $30 \mu\text{atm}$, respectively. Then we address the global validation using all available cruises during these years.

We summarize in Table 4 the results of the computations of the errors given by Eqs. (7)–(10) by making averages over all valid intersections found during 2005, 2006 and 2008. The absolute error, AE is smaller in the three cases of $p\text{CO}_2^{\text{infer}}$ (17.77 , 16.47 and $16.62 \mu\text{atm}$ for OSTIA-MERIS, OSTIA-GLOBCOLOUR and MODIS-GLOBCOLOUR combinations, respectively) than for $p\text{CO}_2^{\text{Ctrack}}$ (21.34 , 22.08 and

Tracker, enhancing the small scale variability. Spatial fluctuations observed in latitudinal profiles of in-situ $p\text{CO}_2$ have been also obtained in the inferred $p\text{CO}_2$, showing that the inferring algorithm is catching the small scales features of the $p\text{CO}_2$ field. The examination of different combinations of Ocean Colour and Sea Surface Temperature (SST) products reveals that using merged products, i.e. GLOBCOLOUR, the quality and the number of valid points in the $p\text{CO}_2$ field are increased. We have obtained that mean absolute errors of the inferred values of $p\text{CO}_2$ with respect to in-situ measurements are smaller than for CarbonTracker.

We are aware that further investigations can be performed in order to improve the algorithm. On one hand the multiple linear regression coefficients could be derived differentiating the seasons (i.e. coefficients would vary as a function of calendar month) considering the marked seasonal cycle in the Benguela upwelling system. Additionally, future works will be focused in the extension of the computations towards larger areas until being able to infer global high resolution CO_2 fluxes. This will allow us to perform an even more comprehensive and robust validation from in situ measurements since more in-situ measurements will be used to make the comparison.

Acknowledgements. This work is a contribution to ESA Support To Science Element Grant No 400014715/11/I-NB OceanFlux-Upwelling Theme.

References

- Abraham, E. and Bowen, M.: Chaotic stirring by a mesoscale surface-ocean flow, *Chaos*, 12, 373–381, 2002. 1408
- Abraham, E., Law, C., Boyd, P., Lavender, S., Maldonado, M., and Bowie, A.: Importance of stirring in the development of an iron-fertilized phytoplankton bloom, *Nature*, 407, 727–730, 2000. 1408
- Arneodo, A., Argoul, F., Bacry, E., Elezgaray, J., and Muzy, J. F.: *Ondelettes, Multifractales et Turbulence*, Diderot Editeur, Paris, France, 1995. 1408, 1418
- Bakker, D. C. E., Pfeil, B., Smith, K., Hankin, S., Olsen, A., Alin, S. R., Cosca, C., Harasawa, S., Kozyr, A., Nojiri, Y., O'Brien, K. M., Schuster, U., Telszewski, M., Tilbrook, B., Wada, C.,

Super-resolution CO₂ fluxes from Earth observations

I. Hernández-Carrasco
et al.

Title Page

Abstract

Introduction

Conclusions

References

Tables

Figures



Back

Close

Full Screen / Esc

Printer-friendly Version

Interactive Discussion



Akl, J., Barbero, L., Bates, N. R., Boutin, J., Bozec, Y., Cai, W.-J., Castle, R. D., Chavez, F. P., Chen, L., Chierici, M., Currie, K., de Baar, H. J. W., Evans, W., Feely, R. A., Fransson, A., Gao, Z., Hales, B., Hardman-Mountford, N. J., Hoppema, M., Huang, W.-J., Hunt, C. W., Huss, B., Ichikawa, T., Johannessen, T., Jones, E. M., Jones, S. D., Jutterström, S., Kitidis, V., Körtzinger, A., Landschützer, P., Lauvset, S. K., Lefèvre, N., Manke, A. B., Mathis, J. T., Merlivat, L., Metzl, N., Murata, A., Newberger, T., Omar, A. M., Ono, T., Park, G.-H., Pater-
son, K., Pierrot, D., Ríos, A. F., Sabine, C. L., Saito, S., Salisbury, J., Sarma, V. V. S. S., Schlitzer, R., Sieger, R., Skjelvan, I., Steinhoff, T., Sullivan, K. F., Sun, H., Sutton, A. J., Suzuki, T., Sweeney, C., Takahashi, T., Tjiputra, J., Tsurushima, N., van Heuven, S. M. A. C., Vandemark, D., Vlahos, P., Wallace, D. W. R., Wanninkhof, R., and Watson, A. J.: An up-
date to the Surface Ocean CO₂ Atlas (SOCAT version 2), *Earth Syst. Sci. Data*, 6, 69–90, doi:10.5194/essd-6-69-2014, 2014. 1407

Berti, S. and Lapeyre, G.: Lagrangian reconstructions of temperature and velocity in a model of surface ocean turbulence, *Ocean Model.*, 76, 59–71, 2014. 1409

Bouchet, F. and Venaille, A.: Statistical mechanics of two-dimensional and geophysical flows, *Phys. Rep.*, 515, 227–295, 2012. 1408

Delcroix, T., Alory, G., Cravatte, S., Correge, T., and McPhaden, M.: A gridded sea surface salinity dataset for the tropical Pacific with sample applications (1950–2008), *Deep-Sea Res. Pt. I*, 58, 38–48, 2011. 1411

Dickey, T.: Emerging ocean observations for interdisciplinary data assimilation systems, *J. Marine Syst.*, 40–41, 5–48, 2003. 1407

Donlon, C. J., Martin, M., Stark, J., Roberts-Jones, J., Fiedler, E., and Wimmer, W.: The Operational Sea Surface Temperature and Sea Ice Analysis (OSTIA) system, *Remote Sens. Environ.*, 116, 140–158, 2012. 1414

Franco, A. C., Hernández-Ayón, J. M., Beier, E., Garçon, V., Maske, H., Paulmier, A., Färber-Lorda, J., Castro, R., and Sosa-Ávalos, R.: Air–sea CO₂ fluxes above the stratified oxygen minimum zone in the coastal region off Mexico, *J. Geophys. Res.-Oceans*, 119, 2923–2937, 2014. 1407

Frisch, U.: *Turbulence: The Legacy of A.N. Kolmogorov*, Cambridge University Press, New York, USA, 1995. 1408, 1416

Garbe, C. and Vihharev, J.: Modeling of atmospheric transport of chemical species in the Polar regions, in: *IEEE International Geoscience and Remote Sensing Symposium*, IEEE, Munich, Germany, 6047–6050, 22–27 July, 2012. 1408, 1410, 1411, 1412

Super-resolution CO₂ fluxes from Earth observations

I. Hernández-Carrasco
et al.

Title Page

Abstract

Introduction

Conclusions

References

Tables

Figures



Back

Close

Full Screen / Esc

Printer-friendly Version

Interactive Discussion



- Garbe, C., Handler, R. A., and Jahne, B.: Transport at the Air–Sea Interface – Measurements, Models and Parameterizations, Springer-Verlag, Berlin, ISBN: 978-3-540-36904-2, 2007. 1410
- Garbe, C., Rutgersson, A., Boutin, J., Delille, B., Fairall, C., Gruber, N., Hare, J., Ho, D., Johnson, M., de Leeuw, G., Nightingale, P., Pettersson, H., Piskozub, J., Sahlee, E., Tsai, W., Ward, B., Woolf, D., and Zappa, C.: Transfer across the air–sea interface, in: Ocean–Atmosphere Interactions of Gases and Particles, edited by: Liss, P. and Johnson, M., Springer-Verlag, Norwich, UK, 55–112, 2014. 1410
- González-Dávila, M., Santana-Casano, J., and Ucha, I.: Seasonal variability of $f\text{CO}_2$ in the Angola-Benguela region, *Prog. Oceanogr.*, 83, 124–133, 2009. 1410, 1415
- Gruber, N., Gloor, M., Mikaloff Fletcher, S. E., Doney, S. C., Dutkiewicz, S., Follows, M. J., Gerber, M., Jacobson, A. R., Joos, F., Lindsay, K., Menemenlis, D., Mouchet, A., Muller, S. A., Sarmiento, J. L., and Takahashi, T.: Oceanic sources, sinks and transport of atmospheric CO₂, *Global Biogeochem. Cy.*, 23, GB1005, doi:10.1029/2008GB003349, 2009. 1407
- Gutknecht, E., Dadou, I., Marchesiello, P., Cambon, G., Le Vu, B., Sudre, J., Garçon, V., Machu, E., Rixen, T., Kock, A., Flohr, A., Paulmier, A., and Lavik, G.: Nitrogen transfers off Walvis Bay: a 3-D coupled physical/biogeochemical modeling approach in the Namibian upwelling system, *Biogeosciences*, 10, 4117–4135, doi:10.5194/bg-10-4117-2013, 2013. 1417
- Hales, B., Takahashi, T., and Bandstra, L.: Atmospheric CO₂ uptake by a coastal upwelling system, *Global Biogeochem. Cy.*, 19, GB1009, doi:10.1029/2004GB002295, 2005. 1409
- IOCCP: Surface Ocean CO₂ Variability and Vulnerabilities Workshop, Rep. 7, U.N. Educ., Sci., and Cult. Organ., Paris, 5, 2007. 1407
- Klein, P. and Lapeyre, G.: The oceanic vertical pump induced by mesoscale and submesoscale turbulence, *Annu. Rev. Mar. Sci.*, 1, 351–75, 2009. 1407
- Mahadevan, A., Lévy, M., and Mémerly, L.: Mesoscale variability of sea surface $p\text{CO}_2$: what does it respond to?, *Global Biogeochem. Cy.*, 18, GB1017, doi:10.1029/2003GB002102, 2004. 1407
- Maji, S. K. and Yahia, H. M.: Edges, transitions and criticality, *Pattern Recogn.*, 47, 2104–2115, 2014. 1416
- Maritorena, S. and Siegel, D. A.: Consistent merging of satellite ocean color data sets using a bio-optical model, *Remote Sens. Environ.*, 94, 429–440, 2005. 1413

Super-resolution CO₂ fluxes from Earth observations

I. Hernández-Carrasco
et al.

Title Page

Abstract

Introduction

Conclusions

References

Tables

Figures



Back

Close

Full Screen / Esc

Printer-friendly Version

Interactive Discussion



- Monteiro, P.: Eastern boundary currents: the Benguela Current System, in: Carbon and Nutrient Fluxes in Continental Margins: a Global Synthesis, Chap. 2, edited by: Liu, K., Atkinson, L., Quiñones, R., and Talaue-McManus, L., Springer, Berlin, 64–77, 2010. 1409
- Montes, I., Dewitte, B., Gutknecht, E., Paulmier, A., Dadou, I., Oschlies, A., and Garçon, V.: High-resolution modeling of the Eastern Tropical Pacific Oxygen Minimum Zone: sensitivity to the tropical oceanic circulation, *J. Geophys. Res.-Oceans*, 119, 5515–5532, doi:10.1002/2014JC009858, 2015. 1417
- Paulmier, A., Ruiz-Pino, D., and Garçon, V.: The Oxygen Minimum Zone (OMZ) off Chile as intense source of CO₂ and N₂O, *Cont. Shelf. Res.*, 28, 2746–2756, 2008. 1407
- Paulmier, A., Ruiz-Pino, D., and Garçon, V.: CO₂ maximum in the oxygen minimum zone (OMZ), *Biogeosciences*, 8, 239–252, doi:10.5194/bg-8-239-2011, 2011. 1409
- Peters, W., Jacobson, A. R., Sweeney, C., Andrews, A. E., Conway, T. J., Masarie, K., Miller, J. B., Bruhwiler, L. M. P., Petron, G., Hirsch, A. I., Worthy, D. E. J., van der Werf, G. R., Randerson, J. T., Wennberg, P. O., Krol, M. C., and Tans, P. P.: An atmospheric perspective on North American carbon dioxide exchange: CarbonTracker, *P. Natl. Acad. Sci. USA*, 104, 18925–18930, 2007. 1408, 1411
- Pfeil, B., Olsen, A., Bakker, D. C. E., Hankin, S., Koyuk, H., Kozyr, A., Malczyk, J., Manke, A., Metzl, N., Sabine, C. L., Akl, J., Alin, S. R., Bates, N., Bellerby, R. G. J., Borges, A., Boutin, J., Brown, P. J., Cai, W.-J., Chavez, F. P., Chen, A., Cosca, C., Fassbender, A. J., Feely, R. A., González-Dávila, M., Goyet, C., Hales, B., Hardman-Mountford, N., Heinze, C., Hood, M., Hoppema, M., Hunt, C. W., Hydes, D., Ishii, M., Johannessen, T., Jones, S. D., Key, R. M., Körtzinger, A., Landschützer, P., Lauvset, S. K., Lefèvre, N., Lenton, A., Lourantou, A., Merlivat, L., Midorikawa, T., Mintrop, L., Miyazaki, C., Murata, A., Nakadate, A., Nakano, Y., Nakaoka, S., Nojiri, Y., Omar, A. M., Padin, X. A., Park, G.-H., Paterson, K., Perez, F. F., Pierrot, D., Poisson, A., Ríos, A. F., Santana-Casiano, J. M., Salisbury, J., Sarma, V. V. S. S., Schlitzer, R., Schneider, B., Schuster, U., Sieger, R., Skjelvan, I., Steinhoff, T., Suzuki, T., Takahashi, T., Tedesco, K., Telszewski, M., Thomas, H., Tilbrook, B., Tjiputra, J., Vandemark, D., Veness, T., Wanninkhof, R., Watson, A. J., Weiss, R., Wong, C. S., and Yoshikawa-Inoue, H.: A uniform, quality controlled Surface Ocean CO₂ Atlas (SOCAT), *Earth Syst. Sci. Data*, 5, 125–143, doi:10.5194/essd-5-125-2013, 2013. 1407
- Pont, O., Turiel, A., and Pérez-Vicente, C. J.: On optimal wavelet bases for the realization of microcanonical cascade processes, *Int. J. Wavelets Multi.*, 9, 35–61, 2011a. 1419

Super-resolution CO₂ fluxes from Earth observations

I. Hernández-Carrasco
et al.

Title Page

Abstract

Introduction

Conclusions

References

Tables

Figures

◀

▶

◀

▶

Back

Close

Full Screen / Esc

Printer-friendly Version

Interactive Discussion



based on climatological surface ocean $p\text{CO}_2$, and seasonal biological and temperature effects, *Deep-Sea Res. Pt. II*, 49, 1601–1622, 2002. 1407

Takahashi, T., Sutherland, S. C., Sweeney, C., Feely, R. A., Chipman, D. W., Hales, B., Friederich, G., Chavez, F., Sabine, C., Watson, A., Bakker, D. C. E., Schuster, U., Metzl, N., Yoshikawa-Inoue, H., Ishii, M., Midorikawa, T., Nojiri, Y., Kortzinger, A., Steinhoff, T., Hoppema, M., Olafsson, J., Anarson, T. S., Tilbrook, B., Johannessen, T., Olsen, A., Bellerby, R., Wong, C. S., Delille, B., Bates, N. R., and de Baar, H. J. W.: Climatological mean and decadal change in surface ocean $p\text{CO}_2$, and net sea–air CO₂ flux over the global oceans, *Deep-Sea Res. Pt. II*, 56, 554–577, 2009. 1407

Turiel, A., Isern-Fontanet, J., García-Ladona, E., and Font, J.: Multifractal method for the instantaneous evaluation of the stream function in geophysical flows, *Phys. Rev. Lett.*, 95, 1–4, 2005. 1408, 1416

Turiel, A., Yahia, H., and Pérez-Vicente, C.: Microcanonical multifractal formalism—a geometrical approach to multifractal systems: Part I. Singularity analysis., *J. Phys. A-Math. Theor.*, 41, 015501–015536, 2008. 1416, 1418

Valsala, V. and Maksyutov, S.: Simulation and assimilation of global ocean $p\text{CO}_2$ and air–sea CO₂ fluxes using ship observations of surface ocean $p\text{CO}_2$ in a simplified biogeochemical offline model, *Tellus B*, 62, 821–840, 2010. 1408

Waldron, H. N., Monteiro, P. M. S., and Swart, N. C.: Carbon export and sequestration in the southern Benguela upwelling system: lower and upper estimates, *Ocean Sci.*, 5, 711–718, doi:10.5194/os-5-711-2009, 2009. 1409

Weiss, R.: Carbon dioxide in water and seawater: the solubility of a non-ideal gas, *Mar. Chem.*, 2, 203–215, 1974. 1411

Yahia, H., Sudre, J., Pottier, C., and Garçon, V.: Motion analysis in oceanographic satellite images using multiscale methods and the energy cascade, *Pattern Recogn.*, 43, 3591–3604, 2010. 1408, 1419

Super-resolution CO₂ fluxes from Earth observations

I. Hernández-Carrasco
et al.

Title Page

Abstract

Introduction

Conclusions

References

Tables

Figures



Back

Close

Full Screen / Esc

Printer-friendly Version

Interactive Discussion



Table 1. Values of the SD, skewness and kurtosis for the different products.

PRODUCT	SD	Skewness	Kurtosis
MERIS	0.116 mg m ⁻³	2.6	21.9
GLOBCOLOUR-AVW	0.122 mg m ⁻³	4.7	204.6
GLOBCOLOUR-GSM	0.123 mg m ⁻³	5.3	215.4
OSTIA	1.97 °C	-0.05	1.9
MODIS	2.11 °C	-0.17	2.6

Super-resolution CO₂ fluxes from Earth observations

I. Hernández-Carrasco
et al.

Title Page

Abstract

Introduction

Conclusions

References

Tables

Figures



Back

Close

Full Screen / Esc

Printer-friendly Version

Interactive Discussion



Table 2. Values of the SD, skewness and kurtosis of the singularity exponents for the different products.

PRODUCT	SD	Skewness	Kurtosis
MERIS	0.32 mg m ⁻³	0.59	3.1
GLOBCOLOUR-AVW	0.36 mg m ⁻³	0.40	3.1
GLOBCOLOUR-GSM	0.35 mg m ⁻³	0.63	4.3
OSTIA	0.29 °C	1.0	5.1
MODIS	0.32 °C	0.5	3.2

Super-resolution CO₂ fluxes from Earth observations

I. Hernández-Carrasco
et al.

Title Page

Abstract

Introduction

Conclusions

References

Tables

Figures

◀

▶

◀

▶

Back

Close

Full Screen / Esc

Printer-friendly Version

Interactive Discussion



Table 3. Number of valid points in the $p\text{CO}_2$ fields and their difference between the three combinations of MERIS or GLOBCOLOUR CHL with OSTIA or MODIS SST in the area of Benguela.

Valid Points in the inferred $p\text{CO}_2$ fields: 2006/08	
No total pixels domain	55 711 378
No Points OSTIA-MERIS	9 800 776
No Points OSTIA-GLOBCOLOUR(AVW)	26 382 072
No Points OSTIA-GLOBCOLOUR(GSM)	27 313 043
No Points MODIS-GLOBCOLOUR(GSM)	20 397 047
Proportion OSTIA-GSM/OSTIA-MERIS	2.78
Proportion OSTIA-GSM/MODIS-GSM	1.33
Proportion MODIS-GSM-/OSTIA-MERIS	1.08
LP _{OM}	82 %
LP _{OG} (AVW)	53 %
LP _{OG} (GSM)	51 %
LP _{MG}	63 %

Super-resolution CO₂ fluxes from Earth observations

I. Hernández-Carrasco
et al.

Table 4. Mean error, absolute error and relative error of $p\text{CO}_2$ values obtained from Carbon-Tracker and $p\text{CO}_2$ values inferred at super-resolution with respect to values of $p\text{CO}_2$ measurements during the QUIMA2005/QUIMA2006/QUIMA2008 cruises in the Benguela region.

	OST-MER	OST-GLOB	MOD-GLOB
No valid intersections	747	1928	1460
L_{infer} (%)	91	76	82
$\text{ME}_{\text{ctrack}}$ (μatm)	2.97	8.83	14.93
ME_{infer} (μatm)	0.15	3.42	8.42
$\text{AE}_{\text{ctrack}}$ (μatm)	21.34	22.08	22.07
AE_{infer} (μatm)	17.77	16.47	16.62
$\text{RE}_{\text{ctrack}}$	0.059	0.060	0.061
RE_{infer}	0.048	0.045	0.046

[Title Page](#)
[Abstract](#)
[Introduction](#)
[Conclusions](#)
[References](#)
[Tables](#)
[Figures](#)
[Back](#)
[Close](#)
[Full Screen / Esc](#)
[Printer-friendly Version](#)
[Interactive Discussion](#)


Super-resolution CO₂ fluxes from Earth observations

I. Hernández-Carrasco
et al.

Table 5. Mean error, absolute error and relative error of $p\text{CO}_2$ values obtained from Carbon-Tracker and $p\text{CO}_2$ values inferred at super-resolution with respect to values of $p\text{CO}_2$ measurements during the QUIMA2005/QUIMA2006/QUIMA2008 cruises in the Benguela region at the same intersections.

	OST-MER	OST-GLOB	MOD-GLOB
No valid intersections	458	458	458
ME _{Track} (μatm)	8.01	8.01	8.01
ME _{infer} (μatm)	4.37	1.62	3.32
AE _{Track} (μatm)	23.23	23.23	23.23
AE _{infer} (μatm)	19.92	16.31	18.85
RE _{Track}	0.065	0.065	0.065
RE _{infer}	0.055	0.045	0.051

[Title Page](#)
[Abstract](#)
[Introduction](#)
[Conclusions](#)
[References](#)
[Tables](#)
[Figures](#)
[Back](#)
[Close](#)
[Full Screen / Esc](#)
[Printer-friendly Version](#)
[Interactive Discussion](#)


Super-resolution CO₂ fluxes from Earth observations

I. Hernández-Carrasco et al.

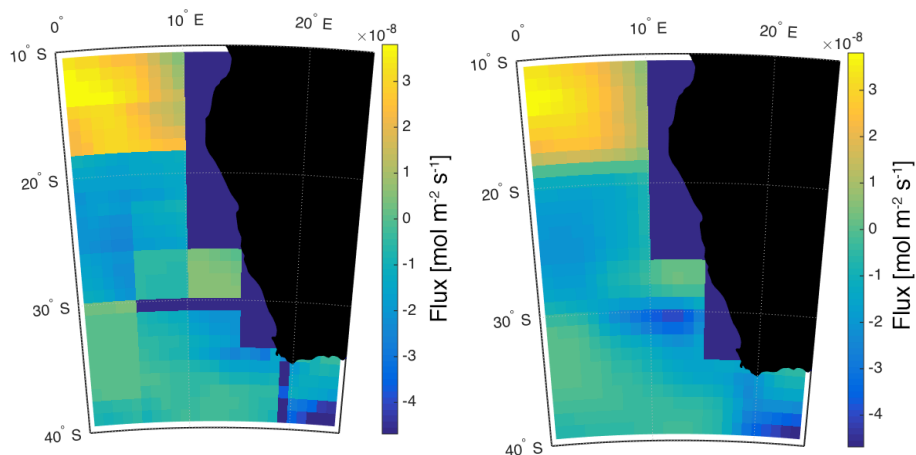


Figure 1. Estimated fluxes from CarbonTracker data. Shown are the results on the Benguela upwelling system on 23 March 2006. Left are the CarbonTracker fluxes, right are our results.

[Title Page](#)[Abstract](#)[Introduction](#)[Conclusions](#)[References](#)[Tables](#)[Figures](#)[⏪](#)[⏩](#)[◀](#)[▶](#)[Back](#)[Close](#)[Full Screen / Esc](#)[Printer-friendly Version](#)[Interactive Discussion](#)

Super-resolution CO₂ fluxes from Earth observations

I. Hernández-Carrasco et al.

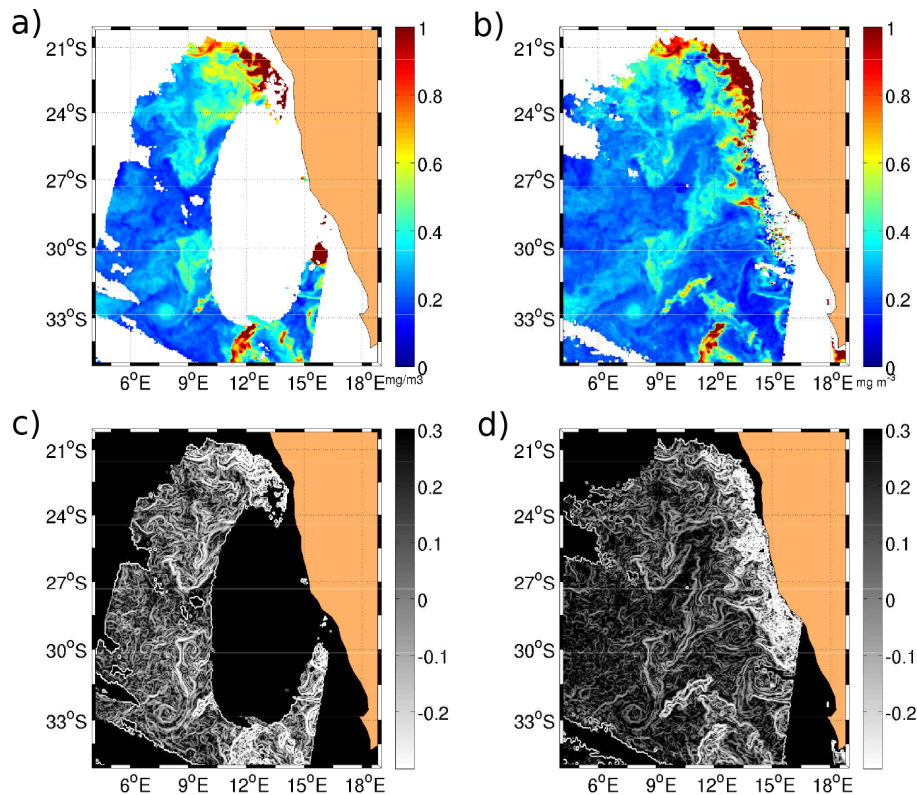


Figure 2. Snapshot of Chl *a* fields corresponding to 21 September 2006 at $1/32^\circ$ from MERIS (a) and GSM GLOBCOLOUR (b). (c and d) are the spatial distribution of Singularity Exponents of the Chl *a* plotted in (a and b) respectively.

[Title Page](#)
[Abstract](#)
[Introduction](#)
[Conclusions](#)
[References](#)
[Tables](#)
[Figures](#)
[⏪](#)
[⏩](#)
[◀](#)
[▶](#)
[Back](#)
[Close](#)
[Full Screen / Esc](#)
[Printer-friendly Version](#)
[Interactive Discussion](#)


Super-resolution CO₂ fluxes from Earth observations

I. Hernández-Carrasco et al.

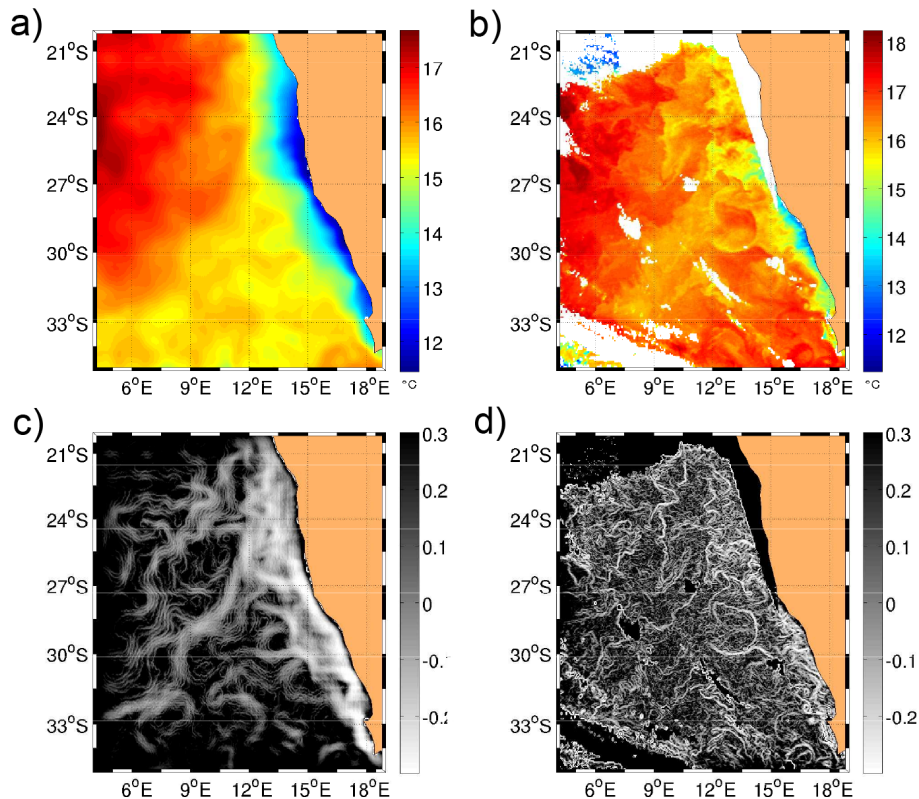


Figure 3. Snapshot of SST fields corresponding to 21 September 2006 regridded at $1/32^\circ$ of spatial resolution from OSTIA (a) and MODIS (b). (c and d) are the spatial distribution of Singularity Exponents of the SST plotted in (a and b) respectively.

Title Page

Abstract

Introduction

Conclusions

References

Tables

Figures

◀

▶

◀

▶

Back

Close

Full Screen / Esc

Printer-friendly Version

Interactive Discussion



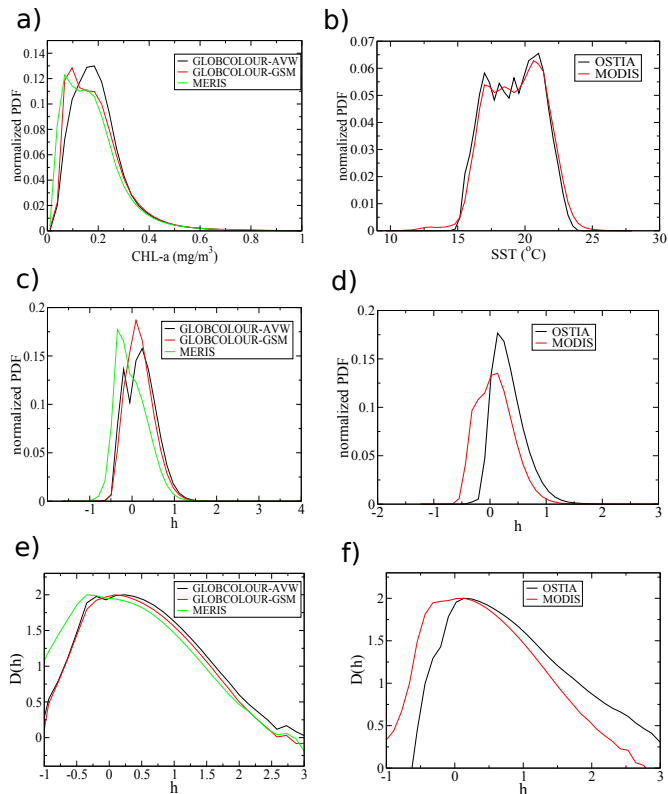


Figure 4. (a) Probability distribution functions (PDF) of Chl *a* values derived from the three products: MERIS, GLOBCOLOUR-AVW and GLOBCOLOUR-GSM. (b) PDF of SST values for OSTIA and MODIS products. (c) PDFs for the singularity exponents of Chl for the different Ocean Colour products. (d) PDFs for the singularity exponents of Chl for the different SST products. (e) Singularity spectra corresponding to (c). (f) Singularity spectra corresponding to (d).

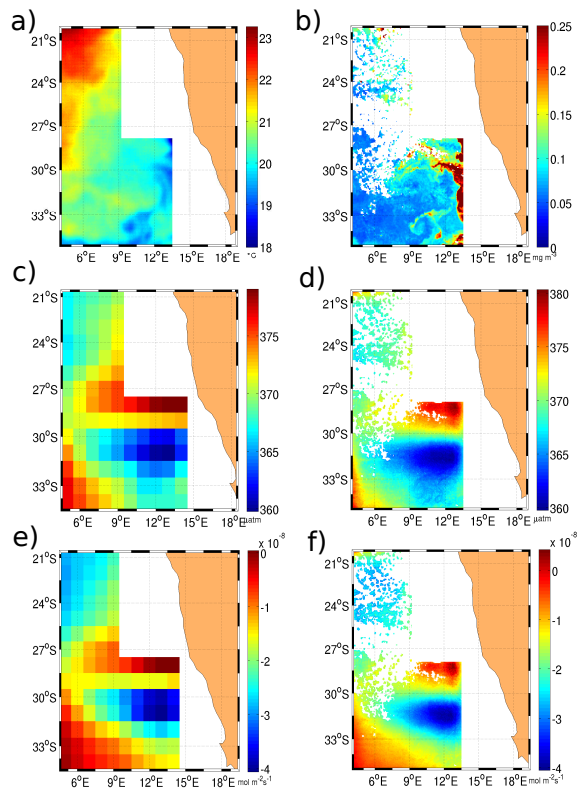


Figure 5. Maps of **(a)** SST from OSTIA at 1/32° of spatial resolution, **(b)** Chl at 1/32° of spatial resolution from GSM GLOBSCOLOUR products, **(c)** ocean $p\text{CO}_2$ from CarbonTracker at the spatial resolution of 1°, **(d)** inferred $p\text{CO}_2$ at super-resolution (1/32°) derived from OSTIA SST and GLOBSCOLOUR-GSM Chl a shown in **(a)** and **(b)** respectively, **(e)** Air–sea CO_2 flux as derived from CarbonTracker and **(f)** Air–sea CO_2 flux computed from super-resolution $p\text{CO}_2$ shown in **(d)** at 1/32°. All images correspond to 22 March 2006. White color corresponds to invalid pixels due to cloudiness and points inside of the CarbonTracker land mask.

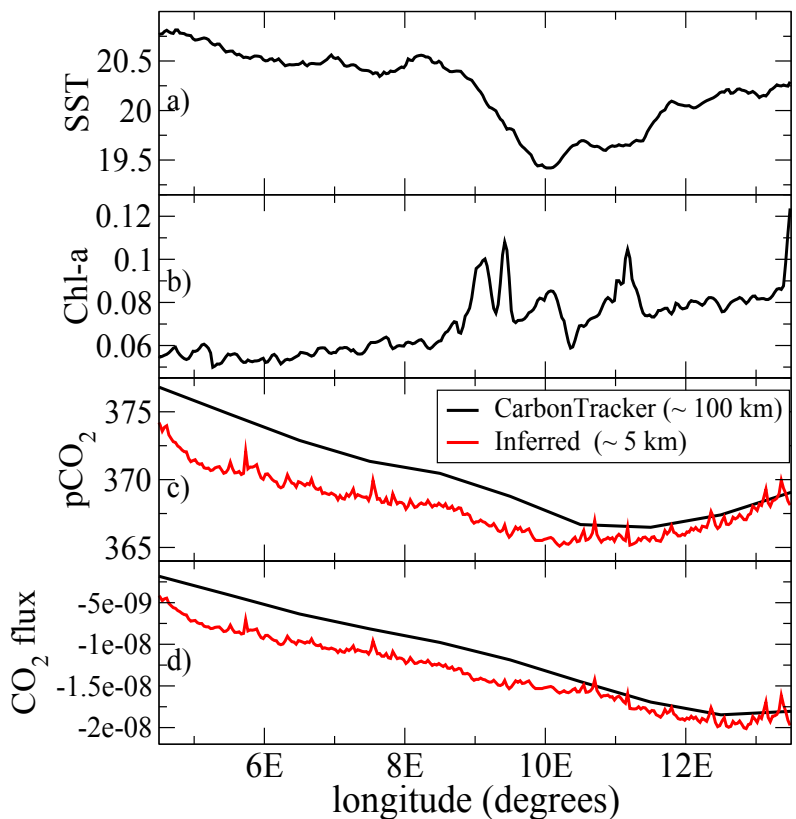


Figure 6. Longitudinal profiles of **(a)** SST from OSTIA products in units of °C, **(b)** Chl from GLOBCOLOUR-GSM ocean in mgm^{-3} , **(c)** $p\text{CO}_2$ from CarbonTracker air–sea fluxes (black line) and inferred $p\text{CO}_2$ (red line) in μatm , and **(d)** air–sea CO_2 fluxes from CarbonTracker (black line) and inferred air–sea CO_2 fluxes (red line) in $\text{molCm}^{-2}\text{s}^{-1}$. All these longitudinal profiles correspond to the fixed latitude equal to 33.5°S of the plots shown in Fig. 5 for 22 March 2006.

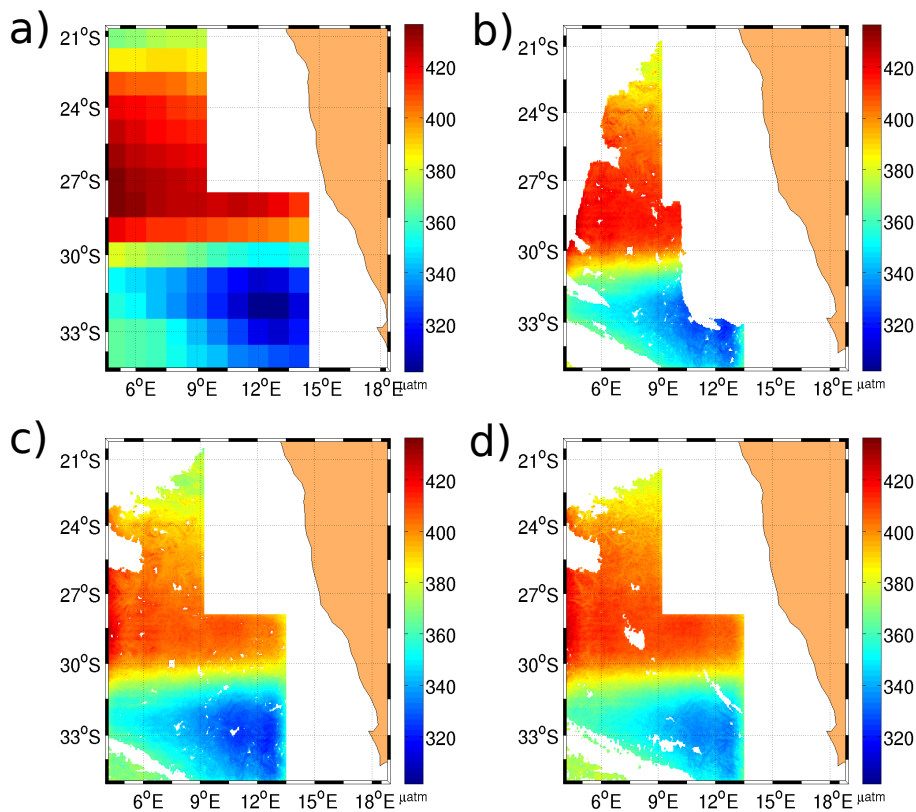


Figure 7. (a) Map of $p\text{CO}_2$ field at low resolution from CarbonTracker. Reconstructed $p\text{CO}_2$ field at super-resolution using: (b) OSTIA SST and MERIS Chl a , (c) OSTIA SST and GSM-GLOBCOLOUR Chl a and (d) MODIS SST and GSM-GLOBCOLOUR Chl a . All maps correspond to 21 September 2006.

Title Page

Abstract

Introduction

Conclusions

References

Tables

Figures

◀

▶

◀

▶

Back

Close

Full Screen / Esc

Printer-friendly Version

Interactive Discussion



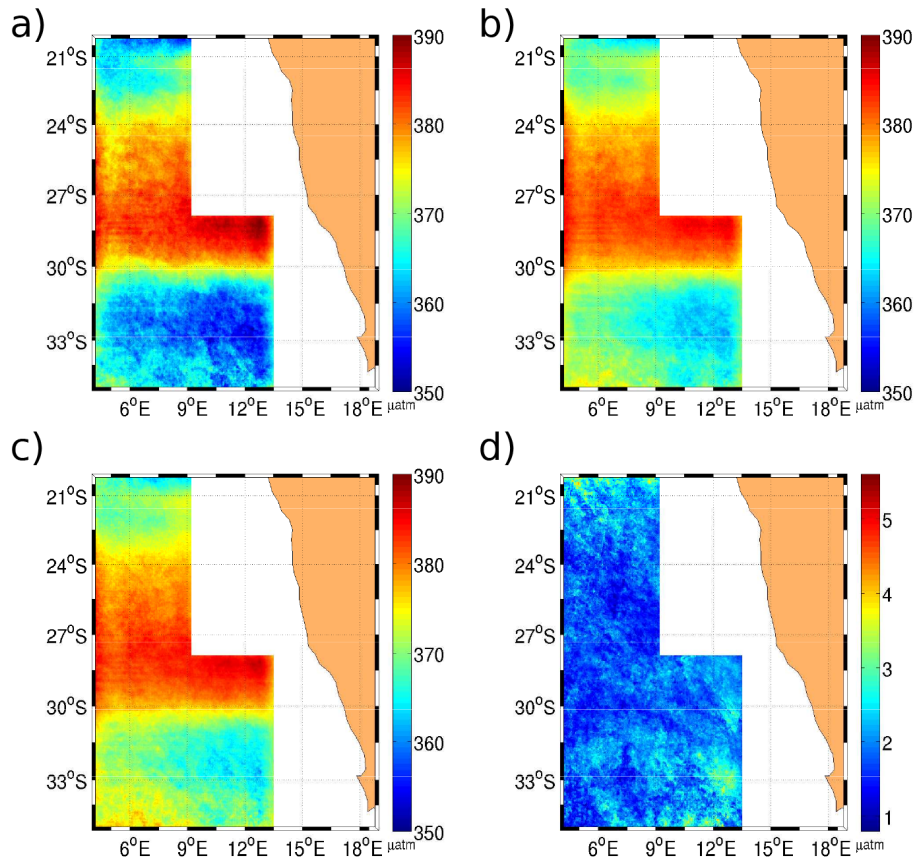


Figure 8. Spatial distribution of the time average over both 2006 and 2008 years of the inferred $p\text{CO}_2$ values using: **(a)** OSTIA SST and MERIS Chl a , **(b)** OSTIA SST and GSM-GLOBCOLOUR Chl a and **(c)** MODIS SST and GSM-GLOBCOLOUR Chl a . **(d)** Map with spatial distribution of the SD for the inferred $p\text{CO}_2$ among the different combination of the datasets.

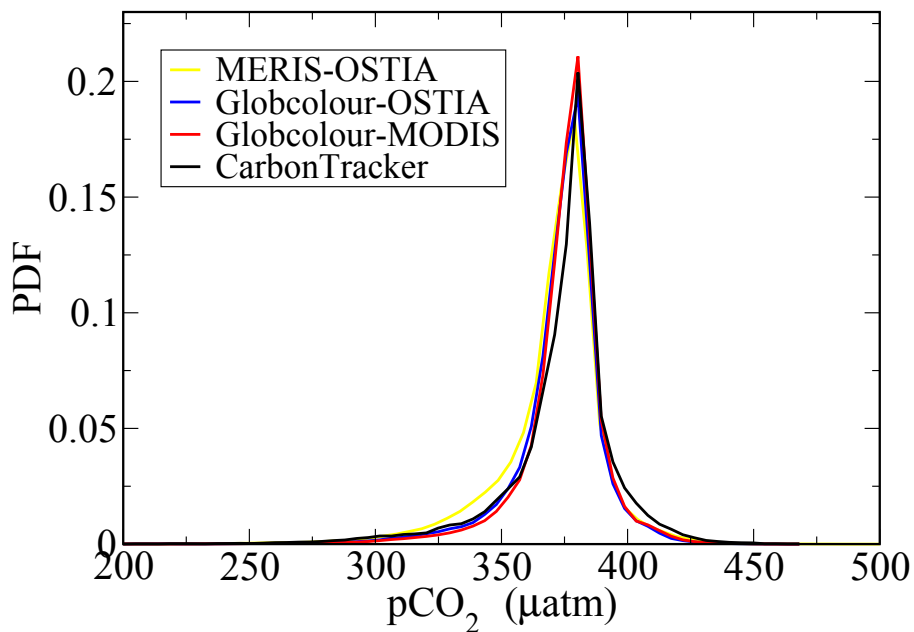


Figure 9. Comparison of the Probability Distribution Functions of CarbonTracker and inferred $p\text{CO}_2$ values over the Benguela area for the three different SST and OC product combinations: MERIS Chl and OSTIA SST, GLOBCOLOUR merged Chl and OSTIA SST, and GLOBCOLOUR merged Chl and MODIS SST.

Super-resolution CO_2 fluxes from Earth observations

I. Hernández-Carrasco et al.

[Title Page](#)

[Abstract](#) | [Introduction](#)

[Conclusions](#) | [References](#)

[Tables](#) | [Figures](#)

[◀](#) | [▶](#)

[◀](#) | [▶](#)

[Back](#) | [Close](#)

[Full Screen / Esc](#)

[Printer-friendly Version](#)

[Interactive Discussion](#)



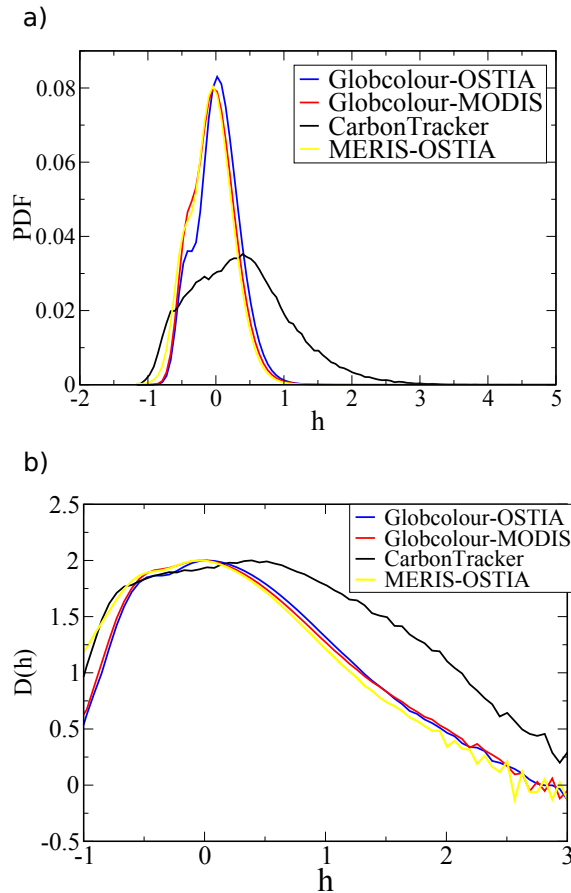


Figure 10. (a) Empirical PDFs for the singularity exponents of $p\text{CO}_2$ fields from CarbonTracker and from the cascade of the three product combinations. (b) Associated singularity spectra. In these computations we use all the $p\text{CO}_2$ values obtained in 2006 and 2008.

Super-resolution CO_2 fluxes from Earth observations

I. Hernández-Carrasco et al.

Title Page

Abstract Introduction

Conclusions References

Tables Figures

◀ ▶

◀ ▶

Back Close

Full Screen / Esc

Printer-friendly Version

Interactive Discussion



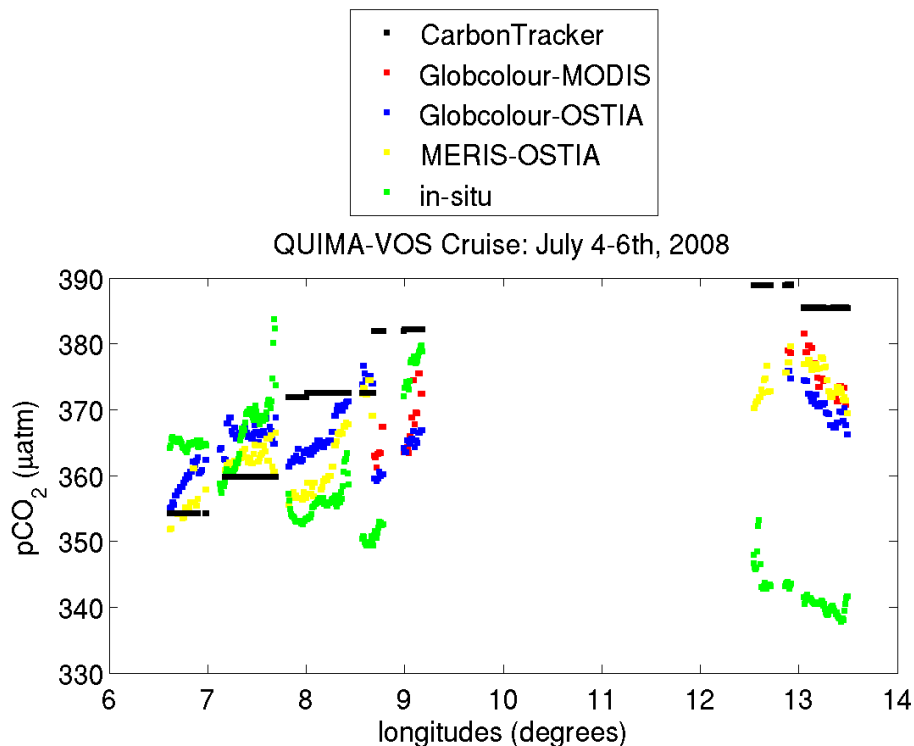


Figure 11. Values of $p\text{CO}_2^{\text{Track}}$ (black points), $p\text{CO}_2^{\text{infer}}$ (MODIS-SST/GLOBCOLOUR-Chl) (red points), $p\text{CO}_2^{\text{infer}}$ (OSTIA-SST/GLOBCOLOUR-Chl) (blue points) $p\text{CO}_2^{\text{infer}}$ (OSTIA-SST/MERIS-Chl) (yellow points) and $p\text{CO}_2^{\text{insitu}}$ (green points) in the intersections as a function of latitude corresponding to the valid intersections during the QUIMA cruise through 4–6 July 2008.

Super-resolution CO₂ fluxes from Earth observations

I. Hernández-Carrasco et al.

[Title Page](#)

[Abstract](#) | [Introduction](#)

[Conclusions](#) | [References](#)

[Tables](#) | [Figures](#)

[◀](#) | [▶](#)

[◀](#) | [▶](#)

[Back](#) | [Close](#)

[Full Screen / Esc](#)

[Printer-friendly Version](#)

[Interactive Discussion](#)

